New Journal of Physics
The open access journal at the forefront of physics

Deutsche Physikalische Gesellschaft DPG IOP Institute of Physics

PAPER • OPEN ACCESS

Quantum oscillations in the type-II Dirac semimetal candidate $PtSe_2$

To cite this article: Hao Yang *et al* 2018 *New J. Phys.* **20** 043008

New Journal of Physics
The open access journal at the forefront of physics

Deutsche Physikalische Gesellschaft DPG
IOP Institute of Physics

Published in partnership with: Deutsche Physikalische Gesellschaft and the Institute of Physics

OPEN ACCESS

RECEIVED
16 November 2017

REVISED
6 February 2018

ACCEPTED FOR PUBLICATION
1 March 2018

PUBLISHED
12 April 2018

PAPER

Quantum oscillations in the type-II Dirac semi-metal candidate $PtSe_2$

Hao Yang[1,2], Marcus Schmidt[1], Vicky Süss[1], Mun Chan[3], Fedor F Balakirev[3], Ross D McDonald[3], Stuart S P Parkin[2], Claudia Felser[1], Binghai Yan[1,4,5] and Philip J W Moll[1,5]

[1] Max-Planck-Institut for Chemical Physics of Solids, D-01187 Dresden, Germany
[2] Max-Planck-Institut of Microstructure Physics, D-06120 Halle, Germany
[3] National High Magnetic Field Laboratory, LANL, MS-E536, Los Alamos, NM 87545, United States of America
[4] Department of Condensed Matter Physics, Weizmann Institute of Science, Rehovot, 7610001, Israel
[5] Authors to whom any correspondence should be addressed.

E-mail: Binghai.Yan@weizmann.ac.il **and** Philip.moll@cpfs.mpg.de

Keywords: Dirac–fermion, transition-metal dichalcogenide, focused ion beam, quantum oscillations, Fermi surface

Abstract

Three-dimensional topological semi-metals carry quasiparticle states that mimic massless relativistic Dirac fermions, elusive particles that have never been observed in nature. As they appear in the solid body, they are not bound to the usual symmetries of space-time and thus new types of fermionic excitations that explicitly violate Lorentz-invariance have been proposed, the so-called type-II Dirac fermions. We investigate the electronic spectrum of the transition-metal dichalcogenide $PtSe_2$ by means of quantum oscillation measurements in fields up to 65 T. The observed Fermi surfaces agree well with the expectations from band structure calculations, that recently predicted a type-II Dirac node to occur in this material. A hole- and an electron-like Fermi surface dominate the semi-metal at the Fermi level. The quasiparticle mass is significantly enhanced over the bare band mass value, likely by phonon renormalization. Our work is consistent with the existence of type-II Dirac nodes in $PtSe_2$, yet the Dirac node is too far below the Fermi level to support free Dirac–fermion excitations.

Introduction

Band structure theory is one of the most successful concepts in condensed matter physics, classifying solids into metals and insulators. One of the key ongoing advances in our understanding of electronic materials is the increasing focus on topological aspects of the electronic bands in the solid [1, 2]. Topological metals and semi-metals are characterized by robust band crossing points near the Fermi energy, leading to linear electronic dispersions in the vicinity of these crossing points. This linear electronic dispersion can be mapped onto the Weyl– and Dirac–Hamiltonian [3, 4] describing massless relativistic fermions. While these have never been observed as elementary particles, in topological materials low energy quasiparticles emerge and mimic these elusive relativistic fermions. Their detection as quasiparticles in condensed matter systems has initiated a fruitful transfer of ideas between these fields of physics, with concepts envisioned for high energy physics now appearing in solids [5, 6]. Recently it was shown that the generalization of the Dirac equation to condensed matter systems also has solutions that cannot appear in elementary particles as they are forbidden by Lorentz symmetry [7]. In general, the dispersion relation in a solid arises due to the interaction of the electrons with the atoms in a periodic crystal, and thereby some of the symmetries of electronic behavior in free space are broken. One example is the appearance of the quasi-momentum of electrons as the translational invariance of free space is replaced by the discrete translation symmetry of the crystal lattice. Similarly in the case of quasiparticles following a massless relativistic dispersion, the rest frame of the crystal lattice defines an absolute frame of reference, and hence Lorentz-invariance is not a symmetry of the electronic system in the solid. This has intriguing consequences: some solutions to the Dirac equation are inherently non-Lorentz-invariant and thus are not allowed for elementary particles. Without Lorentz invariance, these may appear in the solid and new types of relativistic

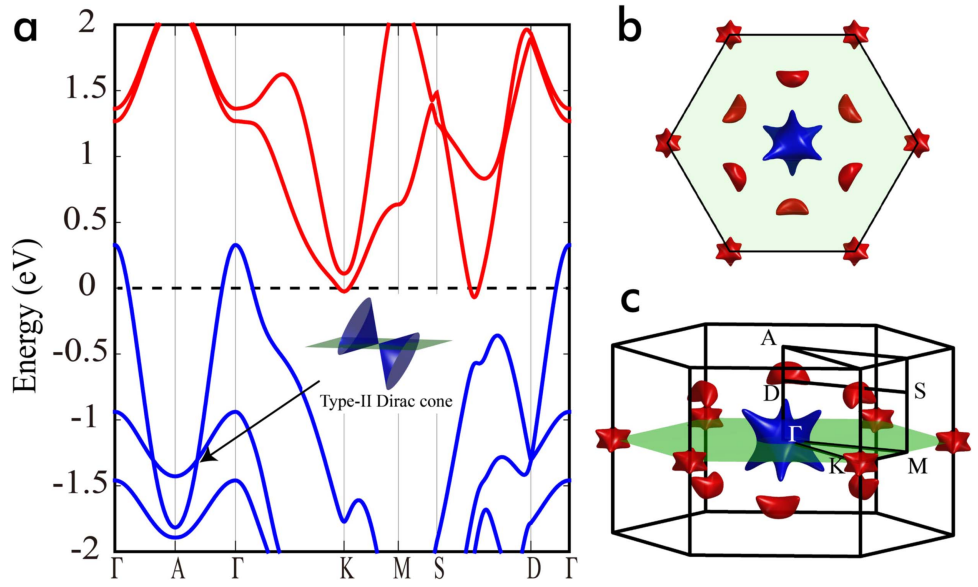

Figure 1. Band structure and type-II Dirac fermions. (a) The band structure along high symmetry lines as shown in (c). Two type-II Dirac points exist at (0 0 $\pm$ 0.317) $\frac{2\pi}{c}$ with energy of 1.30 eV below the Fermi energy. The inset is the 3D plot of the tilted Dirac node. (b) The top and (c) side views of the Fermi surfaces in Brillouin zone. The red and blue pockets correspond to electron and hole pockets, respectively. The bands have been upshifted by 180 meV according to the comparison with the quantum oscillations as discussed in the text.

quasiparticles with a positive Fermi velocity in some, but a negative in other crystal directions are predicted. These are called type-II Dirac nodes that correspond to a singular node at the touching point of an electron- and a hole-type Fermi surface, in contrast to the usual type-I Dirac fermions described by a single definite cone.

The non-degenerate analog, the type-II Weyl semi-metal [7, 8], has been predicted in transition-metal dichalcogenides such as $MoTe_2$. Soon after, these predictions were experimentally verified by imaging the topologically protected Fermi arc surface states via angle-resolved photoemission spectroscopy (ARPES) [9–11]. Recently, a type-II Dirac semi-metal state has been predicted in $PtSe_2$ [12] and successively observed by ARPES studies [13, 14]. The main aim of the present work is to experimentally investigate its electronic structure at the Fermi level via quantum oscillations. In addition to its proposed topological character, $PtSe_2$ is a layered material that has recently attracted attention for its potential use in electronic applications for which a detailed knowledge of the band structure is essential. It can be synthesized in high quality thin film form [15] or as nanocrystallites [16, 17], and it has been proposed as a candidate material for spintronics [18] or electronic applications due to its combination of high electronic mobility, sizeable band-gap and strong spin–orbit coupling.

Band structure calculations

In order to have a direct visualization of the Fermi surface, we have performed first principle calculation using the Vienna *ab initio* simulation package [19]. An 8 $\times$ 8 $\times$ 8 gamma centered grid of k points and a 520 eV plane-wave energy cutoff are adopted for the self-consistent field calculations. The Perdew–Burke–Ernzerhof [20] pseudopotentials with the generalized gradient approximation (GGA) was used in our calculation. In all the calculation, spin orbital coupling are included. We first obtained the band structure of $PtSe_2$ along high symmetry lines as shown in figure 1(a). Along the Γ–A direction, a Dirac-type band crossing is found to reside at 1.30 eV below the Fermi energy at the D point (0 0 0.317) $\frac{2\pi}{c}$, where c is the lattice parameter along z direction. The Dirac node (point D) tilts strongly along k_z (the Γ–D–A line) but only weakly in the k_x–k_y plane (e.g. the S–D line). Our result is fully consistent with [12], predicting a type-II Dirac node as shown in the inset of figure 1(a). As the Dirac node is far below the Fermi level, Dirac quasiparticle excitations are not expected to occur and the transport properties are dominated by non-topological electrons.

To compare these calculations to quantum oscillations arising from these charge carriers at the Fermi level, we have calculated the three-dimensional Fermi surfaces of bulk $PtSe_2$. The Fermi surface consists of three main pockets, one hole-like and two electron-like. The shape of the hole pocket resembles an octahedron, shown in blue in figure 1. The electron bands exhibit two types of Fermi pockets (colored red in figure 1): an octahedron-like electron pocket located around the K point and six crescent-like electron pockets located between D and S points. Both the electron pockets and the hole pocket show three-fold rotation symmetry and inversion

symmetry around the Γ-point, consistent with the symmetry of the crystal structure. Since GGA usually underestimates the gap between conduction and valence bands, we should note that we applied an upshift of 0.18 eV for all conduction bands in figure 1. As discussed below, this constant shift matches the entire angle dependence of the quantum oscillation spectrum well.

Device fabrication

To meaningfully analyze quantum oscillations in metals with non-spherical Fermi surfaces, it is critical to measure an individual single crystal. Highest quality $PtSe_2$ is grown by chemical vapor transport. Yet the resulting crystals often suffer from intergrowth of smaller crystallites, rendering the sample effectively polycrystalline. Therefore we use focused ion beam (FIB) machining to selectively fabricate transport devices from pristine regions of the crystal, to access its true single crystal physics.

The starting material for the microstructure fabrication are conventionally grown single crystals of $PtSe_2$. Our single crystal growth procedure follows previous successful synthesis attempts by chemical vapor transport [21] in the system $Pt/Sn/(S, Se)_2$ using iodine as transport agent. The precursor material $PtSe_2$ was synthesized in a first step by direct reaction of the elements platinum (Alfa Aesar 99.95%) and selenium (Alfa Aesar 99.999%) at 500 °C and 650 °C in evacuated fused silica tubes for 5 d. Starting from this microcrystalline powder, $PtSe_2$ crystallized by a chemical transport reaction in a temperature gradient from 850 °C (source) to 750 °C (sink), and a transport agent concentration of 6 mg cm^{-3} iodine (Alfa Aesar 99,998%). The resulting crystals are thin platelets, with typical sizes of ∼200 μm in-plane and <10 μm perpendicular to the plane. The hexagonal crystal structure is well reflected in the morphology of the platelets. Selected crystals were characterized by EDXS, x-ray powder, and x-ray single crystal diffraction.

The crystallites were patterned using FIB micromachining into meandering bar shapes that are ideally suited for precision resistance measurements. A typical microstructure is shown in figure 2(a). The crystals were patterned using a Ga-ion beam at incidence energies of 60 keV and with currents between 1 and 3 nA. Electrical contacts were made by evaporating gold electrodes onto the crystal (colored yellow in figure 2(a)). Two crystals have been patterned into similar shapes and fully characterized, including the quantum oscillation measurements in high fields, and all results were in quantitative agreement.

This approach has two main advantages for the present experiment, sample optimization for pulsed field experiments and the suppression of artefacts due to crystal defects. The shape of the crystal can be precisely trimmed to optimize the total device resistance given the materials natural specific resistivity. Thereby the device resistance can be set to an optimal value in the 10–100 Ω range for pulsed magnetic field measurements. At lower resistance, the accordingly smaller signal-to-noise ratio impedes the measurement of the oscillatory amplitude of the magnetoresistance. At higher resistance, the larger LRC-time constant of the measurement circuit would require to reduce the frequency of the applied ac-current. Yet lower measurement frequencies come close to the typical noise spectrum of a pulsed magnet which extends into the 10–20 kHz range. By proper design of the microstructure, these issues can be avoided and high quality data obtained from a metal regardless of its resistivity. This approach has proven to be a reliable method to fabricate crystalline samples for transport measurements in high magnetic fields in a large variety of different compounds [22, 23]. In addition, the microstructuring also allows to specifically probe the most pristine region of the crystal and to exclude damaged regions from influencing the measurement. The crystal in figure 2(a) depicts such a scenario: a secondary crystallite grew in into the bottom half of the otherwise perfectly regular hexagonal plate. By using the sub-micron precision of the FIB cutting, the active device area can be patterned into the pristine face of a crystal thus completely bypassing the intergrowth regions.

The temperature dependence in zero magnetic field is shown in figure 2(b). $PtSe_2$ is found to be a reasonably good metal with a resistivity of 130 $\mu\Omega$ cm at room temperature and 25 $\mu\Omega$ cm at 2 K. At lowest temperatures, we consistently observe a slight upturn of the resistance in all fabricated microstructures. This is directly related to a weak negative magnetoresistance at very low fields before the large positive magnetoresistance is observed (inset figure 3(a)). Given the topologically trivial nature of the charge carriers at the Fermi level and the isotropic behavior upon changing the angle of the magnetic field with respect to the current path, a topological origin related to the chiral anomaly can be clearly excluded [24]. A likely explanation is weak localization, however no such behavior was observed in previous studies [17] of the low-temperature resistivity of $PtSe_2$. Thus it may also be possible that electronic interactions conspire with the lateral finite size confinement in the microstructure to yield positive corrections to the apparent device resistance due to viscous effects in a hydrodynamic picture of electron transport [25–27]. Clearly future experiments quantifying the resistance variation among samples and microstructure dimensions are required to address this question.

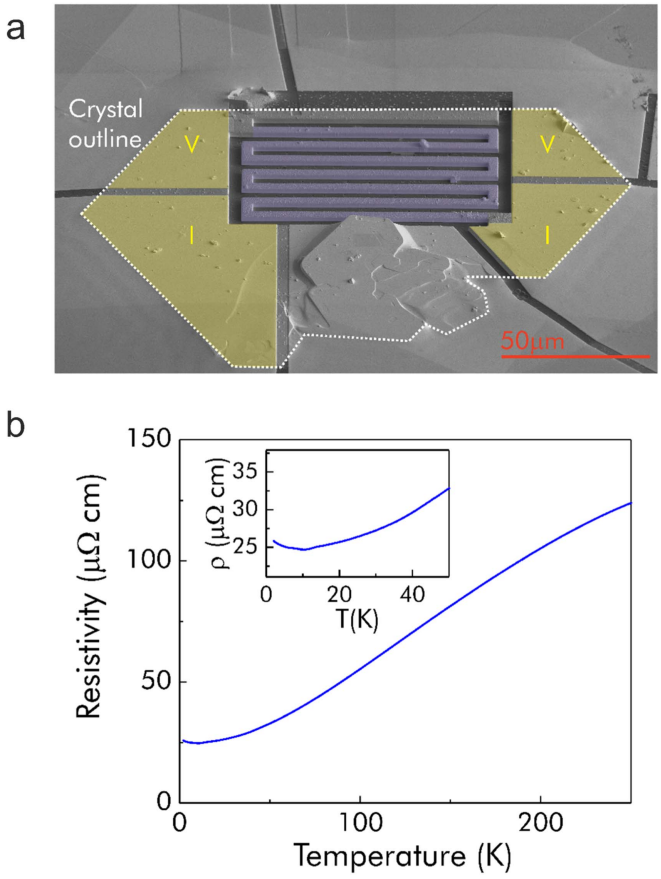

Figure 2. (a) Single crystal microdevice of $PtSe_2$. The meandered resistance path (purple) is the active region of the device where the resistivity is measured. This meander was fabricated in a pristine part of the crystal, avoiding the region of an intergrowth crystal defect. Gold contacts for a four-probe measurement were evaporated onto the crystal by sputter deposition. The meandered path is 3.6 μm wide, 80 μm long and 2 μm deep. (b) Temperature-dependence of the in-plane resistivity, measured in the device shown in (a). The inset shows the low-temperature resistivity and the small upturn observed at lowest temperatures.

Pulsed field magnetoresistance

Angle dependent magnetoresistance measurements were performed at the National High Magnetic Field Laboratory in Los Alamos, using a 65 T short pulse magnet. These high-strength copper solenoids deliver magnetic field pulses with a characteristic time of 8 ms rise time to peak field and a slow fall time from peak field to zero of 100 ms. The magnetoresistance is measured by applying an ac-current of 380 μA at 297.5 kHz to the devices and detecting the voltage response via a lock-in procedure.

The magnetoresistance of $PtSe_2$ at 500 mK increases by a factor of 20 up to 60 T. The family of transition-metal dichalcogenides (TMD) exhibits a wide spectrum of behaviors in high magnetic fields. As in all semi-metals, the magnetoresistance is determined by the Fermi surface shape as well as the degree of compensation between electrons and holes [28]. Some tellurides, such as WTe_2 [29] or $MoTe_2$ [30], exhibit very large and non-saturating magnetoresistance, indicating an almost ideal electron–hole compensation. The electronic structure of $PtSe_2$ is clearly dominated by the central hole band, and the comparatively lower magnetoresistance is expected in light of the poorer electron–hole compensation. The overall magnetoresistance is found to be essentially independent of the angle of the magnetic field to the crystal (figure 3(a)), where 0° corresponds to fields along the [00$\bar{1}$] and 90° along the [110] direction, reflecting the three-dimensional nature of the electronic system.

Fermiology

The magnetoresistance shows pronounced quantum oscillations containing multiple beating frequencies and in general is dominated by two classes of frequencies. The first around 1000 T disperses quickly to higher frequencies upon changing the field angle, indicating a local minimum of the cross-sectional area of this

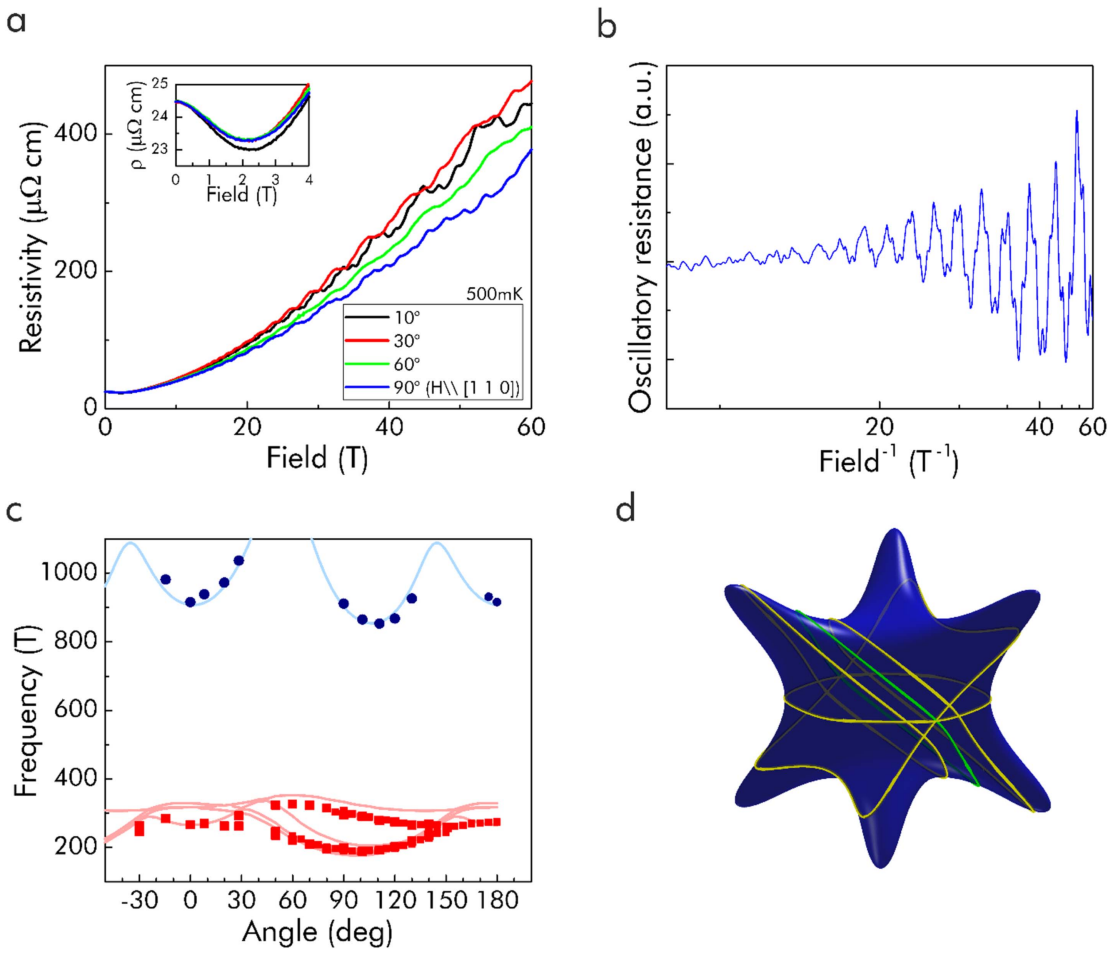

Figure 3. (a) Magnetoresistance of $PtSe_2$ in pulsed fields up to 60 T at 500 mK, for selected field angles. The angle θ defines a plane of rotation as $H \,||\, [00\bar{1}]$ for $\theta = 0°$ and $H \,||\, [110]$ for $\theta = 90°$. (b) Magnetoresistance after subtraction of a smooth polynomial background, plotted against inverse magnetic field. The typical growth of the quantum oscillations as $\omega_c\tau$ increases beyond unity is clearly visible. (c) Angle dependence of the quantum oscillation frequencies in the rotation plane described in (a). Blue denotes the large central hole pocket, and red the smaller electron-like orbits. The measured frequencies (symbols) match well with the band structure calculations (solid lines). (d) Central hole pocket with a few exemplary extremal orbits colored to depict the path of the quasiparticles around the Fermi surface in the quantum oscillation experiment.

quantum orbit ('neck-frequency'). The second set of frequencies belongs to a weakly dispersive frequency band in the 200–300 T range.

The measured frequencies can be directly compared to the band structure calculations. Each frequency corresponds to a separate quantum orbit around the Fermi surface perpendicular to the magnetic field, where figure 3(d) shows an exemplary orbit on the hole pocket. The frequency F is directly proportional to the extremal k-space area S_k enclosed in the orbit, given by the Onsager relation as $F = (\Phi_0/2\pi^2)S_k$, where $\Phi_0 = h/2e$ is the magnetic flux quantum, e the electron charge and h is the Planck constant. We have calculated the quantum oscillation frequencies of electron pockets and hole pocket with the magnetic field rotated from $[00\bar{1}]$ direction to [110] direction. Figure 3(c) displayed both the experimental and calculated quantum oscillation frequencies as a function of the angle between magnetic field and $[00\bar{1}]$ direction. The absence of a mirror plane symmetry perpendicular to the c-direction in the crystal is directly reflected by the lack of symmetry of the quantum oscillation frequency around 90°. The comparison to the band structure calculations allows us to identify the two types of frequencies as orbits on separate Fermi surface sheets. The large frequency belongs to the orbit around a star-shaped hole pocket centered in the Brillouin zone, while the low frequencies belong to the comparatively smaller electron-like Fermi surfaces.

Effective mass enhancement

Quantum oscillations also provide a direct measurement of the quasiparticle effective mass [31]. The temperature dependence of the amplitudes $A(T)$ due to the thermal broadening of the Fermi–Dirac distribution is well described by the Lifshitz–Kosevich formula as $A(T)/A_0 = X/\sinh(X)$, where $X = 2\pi^2 k_B T/\hbar\omega_c$. Here, the cyclotron frequency $\omega_c = \frac{eB}{m^*}$ contains only the quasiparticle effective mass m^* as

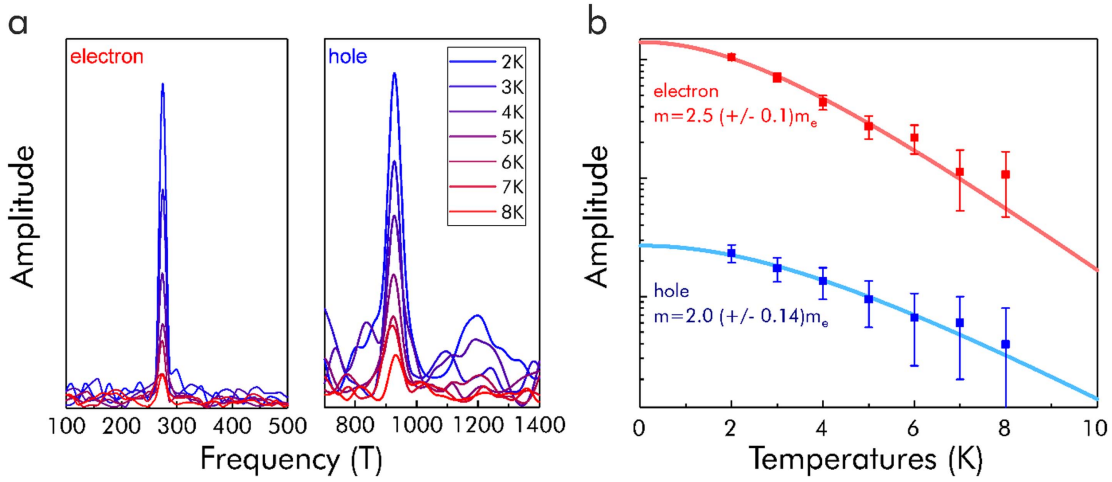

Figure 4. Effective mass. (a) Quantum oscillation frequency spectrum as a function of temperature. Upon increasing temperature, the amplitudes for both orbits decay due to thermal Landau level broadening. (b) Amplitudes for both electron- and hole-like Fermi surfaces as a function of temperature. The measured temperature dependence (symbols) is well described by the Lifshitz–Kosevich formula (straight line), from which the effective mass is extracted as a fitting parameter.

an unknown fitting parameter to the data (figure 4). To extract the amplitude from the raw data, the non-oscillatory part of the magnetoresistance was fitted to a 3rd degree polynomial spline and subtracted from the data, to yield the purely oscillatory component (figure 3(b)). The frequency spectrum in figure 4(a) was obtained by standard Fourier analysis, and the peak height estimated above the experimental noise floor. Both pockets show a similar effective mass, with 2.0($\pm$0.14) m_e for the hole and 2.5($\pm$0.1) m_e for the slightly heavier electron pocket. Here m_e denotes the mass of the free electron. This can be directly compared to the effective mass calculated from the band structure, $m_{\mathrm{band}}(k) = \hbar k/v_{\mathrm{F}}$, which in general is k-dependent. The cyclotron effective mass measured in quantum oscillation experiments is the average effective mass around the quasiparticle orbit, $m^*_{\mathrm{band}} = \frac{1}{L}\oint m_{\mathrm{band}}(\boldsymbol{k})\,\mathrm{d}\boldsymbol{k}$, where L denotes the k-space length of the orbit. The cyclotron effective mass can also be expressed as the change of the k-space area A enclosed by the orbit upon changing the energy E around the Fermi energy, E_{F}, as $m^*_{\mathrm{band}} = \frac{\hbar^2}{2\pi}\left(\frac{\mathrm{d}E}{\mathrm{d}A}\right)^{-1}_{|E_{\mathrm{F}}}$. The latter can be more conveniently calculated from the band structure $E(k)$. For the orbits in the experimental situation of the temperature dependent measurements, $H \,||\, [00\bar{1}]$, a cyclotron mass of $0.4m_e$ is calculated for the hole band, and $0.35m_e$ for the star-shaped electron pocket.

Given the good agreement of the calculated band structure with the measured Fermi surface topology, the most likely explanation for such a sizable disagreement is mass renormalization. When electrons in a solid are coupled to a bosonic field with a strength λ, the quasiparticle dispersion is renormalized as $m^* = (1 + \lambda)m^*_{\mathrm{band}}$. In absence of magnetism in $PtSe_2$, the prime candidate for the origin of the sizable mass enhancement $\lambda \sim 5.5$ is strong electron–phonon coupling [32]. This picture is further supported by recent ARPES experiments finding good agreement between band structure calculations and photoemission spectra over the entire band, thus excluding bandwidth renormalizations due to correlations [13, 14].

Conclusions

The electronic system of the semi-metal $PtSe_2$ is dominated by a larger hole pocket and two small electron pockets, and our results experimentally confirm the band structure calculations of [12]. Thereby our quantum oscillation study provides experimental support for calculated band structures in the TMD that host type-II Dirac fermions. Yet the Dirac node is far below the chemical potential and thus no topological excitations appear in the material. The conductivity and materials properties are therefore dominated by non-topological charge carriers, and promoting the type-II Dirac fermions to the Fermi level is the next important challenge to study their physics and application prospects. Usual methods such as charge doping or gating techniques do not appear as a viable route, given the large energy difference of 1.3 eV between the Dirac node and the Fermi level in $PtSe_2$. Yet it may be possible to find materials in which they reside closer to the Fermi level within the class of TMD layered conductors. Also, recently type-II Dirac fermions closer to the Fermi energy (200–300 meV below E_{F}) were predicted in Heusler compounds [33]. The observed enhancement of the quasiparticle effective mass suggests a strong electron–phonon interaction in $PtSe_2$. The observation of mass enhancement is consistent with the appearance of low-temperature superconductivity in this materials class, such as in the related tellurides

WTe_2 ($T_c \sim 7$ K under pressure [34]) and $MoTe_2$ ($T_c \sim 0.1$ K at ambient pressure, 8.2 K under pressure [35]). This appearance of significant mass renormalization in a topologically non-trivial band structure is of particular interest for the ongoing search for strongly correlated topological materials.

Acknowledgments

We thank Horst Borrmann for the careful crystallographic analysis of the crystals. BY acknowledges the support by the Ruth and Herman Albert Scholars Program for New Scientists in Weizmann Institute of Science, Israel and by a Grant from the GIF, the German-Israeli Foundation for Scientific Research and Development. A portion of this work was completed at the National High Magnetic Field Laboratory's Pulsed Field Facility at Los Alamos National Laboratory, which is supported through National Science Foundation Cooperative Agreement No. DMR 1157490, the Department of Energy and the State of Florida. RDM acknowledges support from LANL LDRD-DR20160085 'Topology and strong correlations'. This project was supported by the European Research Council (ERC) under the European Union's Horizon 2020 research and innovation programme (GA No. 715730).

ORCID iDs

Philip J W Moll https://orcid.org/0000-0002-7616-5886

References

[1] Wehling T O, Black-Schaffer A M and Balatsky A V 2014 Dirac materials *Adv. Phys.* **63** 1–76
[2] Yan B and Felser C 2017 Topological Materials: Weyl Semimetals *Annu. Rev. Condens. Matter Phys.* **8** 337–54
[3] Armitage N P, Mele E J and Vishwanath A 2018 Weyl and Dirac semimetals in three-dimensional solids *Rev. Mod. Phys.* **90** 15001
[4] Novoselov K S *et al* 2005 Two-dimensional gas of massless Dirac fermions in graphene *Nature* **438** 197–200
[5] Dean C R *et al* 2012 Hofstadter's butterfly in moire superlattices: a fractal quantum Hall effect *Nature* **497** 598–602
[6] Katsnelson M I, Novoselov K S and Geim A K 2006 Chiral tunneling and the Klein paradox in graphene *Nat. Phys.* **2** 620–5
[7] Soluyanov A A *et al* 2015 Type-II Weyl semimetals *Nature* **527** 495–8
[8] Sun Y, Wu S C, Ali M N, Felser C and Yan B 2015 Prediction of Weyl semimetal in orthorhombic $MoTe_2$ *Phys. Rev.* B **92** 161107(R)
[9] Huang L *et al* 2016 Spectroscopic evidence for a type-II Weyl semimetallic state in $MoTe_2$ *Nat. Mater.* **15** 1155–60
[10] Deng K *et al* 2016 Experimental observation of topological Fermi arcs in type-II Weyl semimetal $MoTe_2$ *Nat. Phys.* **12** 1105–11
[11] Jiang J *et al* 2016 Signature of type-II Weyl semimetal phase in $MoTe_2$ *Nat. Commun.* **8** 13973
[12] Huang H, Zhou S and Duan W 2016 Type-II Dirac fermions in the $PtSe_2$ class of transition metal dichalcogenides *Phys. Rev.* B **94** 121117
[13] Li Y *et al* 2017 Topological origin of the type-II Dirac fermions in $PtSe_2$ *Phys. Rev. Mater.* **1** 74202
[14] Zhang K *et al* 2017 Experimental evidence for type-II Dirac semimetal in $PtSe_2$ *Phys. Rev.* B **96** 125102
[15] Yim C *et al* 2016 High-performance hybrid electronic devices from layered $PtSe_2$ films grown at low temperature *ACS Nano* **10** 9550–8
[16] Wang Z, Li Q, Besenbacher F and Dong M 2016 Facile synthesis of single crystal $PtSe_2$ nanosheets for nanoscale electronics *Adv. Mater.* **28** 10224–9
[17] Li Z *et al* 2017 Anomalous magnetotransport behaviors in $PtSe_2$ microflakes *J. Phys.: Condens. Matter* **29** 23LT01
[18] Yao W *et al* 2017 Direct observation of spin-layer locking by local Rashba effect in monolayer semiconducting $PtSe_2$ film *Nat. Commun.* **8** 14216
[19] Kresse G and Furthmüller J 1996 Efficiency of *ab-initio* total energy calculations for metals and semiconductors using a plane-wave basis set *Comput. Mater. Sci.* **6** 15–50
[20] Perdew J P, Burke K and Ernzerhof M 1996 Generalized gradient approximation made simple *Phys. Rev. Lett.* **77** 3865–8
[21] Tomm Y, Fiechter S, Diener K and Tributsch H 1997 Phase formation in the system Pt-Sn-(S, Se)2 and crystal growth by chemical vapor transport *Int. Phys. Conf. Ser. No 152 Sect. A, Int. Conf. Ternary Multinary Compd.* pp 167–70
[22] Jaroszynski J *et al* 2008 Upper critical fields and thermally-activated transport of Nd(O0.7F0.3)FeAs single crystal *Phys. Rev.* B **78** 174523
[23] Moll P J W, Zhu X, Cheng P, Wen H-H and Batlogg B 2014 Intrinsic Josephson junctions in the iron-based multi-band superconductor $(V_2Sr_4O_6)Fe_2As_2$ *Nat. Phys.* **10** 644–7
[24] Xiong J *et al* 2015 Evidence for the chiral anomaly in the Dirac semimetal Na_3Bi *Science* **350** 413
[25] Alekseev P S 2016 Negative magnetoresistance in viscous flow of two-dimensional electrons *Phys. Rev. Lett.* **117** 166601
[26] Scaffidi T, Nandi N, Schmidt B, Mackenzie A P and Moore J E 2017 Hydrodynamic electron flow and hall viscosity *Phys. Rev. Lett.* **118** 226601
[27] Moll P J W, Kushwaha P, Nandi N, Schmidt B and Mackenzie A P 2016 Evidence for hydrodynamic electron flow in $PdCoO_2$ *Science* **351** 1061–4
[28] Pippard A B 1989 *Magnetoresistance in Metals* (Cambridge: Cambridge University Press)
[29] Ali M N *et al* 2014 Large non-saturating magnetoresistance in WTe_2 *Nature* **514** 205–8
[30] Chen F C *et al* 2016 Extremely large magnetoresistance in the type-II Weyl semimetal $MoTe_2$ *Phys. Rev.* B **94** 235154
[31] Shoenberg D 1984 *Magnetic Oscillations in Metals* (Cambridge: Cambridge University Press)
[32] Chakraborty B *et al* 2012 Symmetry-dependent phonon renormalization in monolayer MoS_2 transistor *Phys. Rev.* B **85** 161403(R)
[33] Guo P J, Yang H C, Liu K and Lu Z Y 2017 Type-II Dirac semimetals in the YPd_2Sn class *Phys. Rev.* B **95** 155112
[34] Pan X-C *et al* 2015 Pressure-driven dome-shaped superconductivity and electronic structural evolution in tungsten ditelluride *Nat. Commun.* **6** 7805
[35] Qi Y *et al* 2016 Superconductivity in Weyl semimetal candidate $MoTe_2$ *Nat. Commun.* **7** 11038